Research Square

Preprints are preliminary reports that have not undergone peer review.
They should not be considered conclusive, used to inform clinical practice,
or referenced by the media as validated information.

Vessel-resolved MRI reveals the hierarchical organization of brain-wide perivascular tracer transport in vivo

Xiaoqing Zhou
xzhou27@mgh.harvard.edu
Massachusetts General Hospital
Xiaochen Liu
Massachusetts General Hospital
Weitao Man
Massachusetts General Hospital
Sang Cheon Choi
Massachusetts General Hospital
David Hike
Massachusetts General Hospital
Xinyue Wang
Massachusetts General Hospital
Yuanyuan Jiang
Massachusetts General Hospital
Maiken Nedergaard
University of Copenhagen
Kristopher Kahle
Massachusetts General Hospital
Brian Bacskai
Massachusetts General Hospital
Xin Yu
Massachusetts General Hospital

Research Article

Keywords: perivascular spaces, cerebrospinal fluid transport, vessel-resolved MRI, cerebral vasculature, neurofluid dynamics

Posted Date: November 5th, 2026

DOI: https://doi.org/10.21203/rs.3.rs-11393904/v1

License: This work is licensed under a Creative Commons Attribution 4.0 International License.
Read Full License

Additional Declarations: No competing interests reported.

Vessel-resolved MRI reveals the hierarchical organization of brain-wide perivascular tracer transport *in vivo*

Xiaoqing Alice Zhou[1]*, Xiaochen Liu[1], Weitao Man[1], Sang Cheon Choi[1], David Hike[1], Xinyue Wang[1], Yuanyuan Jiang[1], Maiken Nedergaard[2,3], Kristopher T. Kahle[4], Brian Bacskai[5], Xin Yu[1]*

[1]Athinoula A. Martinos Center for Biomedical Imaging, Massachusetts General Hospital, Harvard Medical School, Charlestown, MA, USA

[2]Center for Translational Neuromedicine, University of Copenhagen, Copenhagen, Denmark

[3]Center for Translational Neuromedicine, Division of Glial Disease and Therapeutics, University of Rochester Medical Center, Rochester, NY, USA

[4]Department of Neurosurgery, Massachusetts General Hospital, Harvard Medical School, Boston, Massachusetts, USA

[5]Department of Neurology, Massachusetts General Hospital, Harvard Medical School, Boston, Massachusetts, USA

Corresponding authors: Xiaoqing Alice Zhou and Xin Yu

* Address correspondence to:

Xiaoqing Alice Zhou, Ph.D. and Xin Yu, Ph.D., Athinoula A. Martinos Center for Biomedical Imaging, Massachusetts General Hospital, Harvard Medical School, Charlestown, MA, USA

Email: xzhou27@mgh.harvard.edu, xyu9@mgh.harvard.edu

Abstract

Background: Perivascular tracer transport is thought to support cerebrospinal fluid (CSF) exchange throughout the brain, yet whether this process is organized along defined vascular architectures remains unknown because existing imaging approaches visualize only diffuse tracer distribution or limited local regions.

Methods: Here we combine ultra-high-field MRI, an implantable radiofrequency coil, and dual-contrast imaging to achieve vessel-resolved visualization of brain-wide perivascular tracer transport in vivo.

Results: This approach reveals that perivascular tracer transport is organized hierarchically along vascular trees, extending continuously from major surface arteries into penetrating cortical vessels and deep brain regions, including the hippocampus. Quantitative analyses further show that detectable perivascular tracer transport is restricted to a heterogeneous subset of penetrating vessels, indicating previously unrecognized spatial organization across the cerebral vasculature.

Conclusions: Together, these findings reveal brain-wide perivascular tracer transport as a structured vessel-associated network rather than diffuse tracer accumulation and establish vessel-resolved MRI as an approach for investigating neurofluid organization in health and disease.

Keywords

perivascular spaces; cerebrospinal fluid transport; vessel-resolved MRI; cerebral vasculature; neurofluid dynamics

Background

Perivascular spaces (PVS) are fluid-filled compartments surrounding cerebral vessels and constitute a central anatomical interface for cerebrospinal fluid (CSF) and interstitial fluid (ISF) exchange in the brain(1-3). Within the glymphatic framework, periarterial pathways have been proposed to support CSF influx and solute transport(4), whereas alternative models emphasize intramural periarterial drainage along vascular basement membranes(5-7). Although the relative contributions of these pathways remain debated, there is broad consensus that perivascular compartments play a fundamental role in brain fluid transport, solute clearance, and homeostasis, with dysfunction implicated in aging, cerebrovascular disease, and neurodegeneration(8-10).

Recent work further indicates that CSF-ISF exchange is dynamically regulated by neural, vascular, and autonomic processes rather than passive diffusion alone. Brain state strongly modulates glymphatic transport, with sleep and circadian rhythms influencing fluid exchange and clearance(11). In parallel, increasing evidence demonstrates tight coupling between neuronal activity and CSF dynamics, In particular, coordinated neural oscillations and slow-wave activity can modulate, and in some cases directly drive, brain-wide CSF movement and clearance(12-14).Vascular dynamics also contribute to this process, as arterial pulsations and vasomotion have been implicated in shaping perivascular fluid movement(15), while recent work shows that slow norepinephrine-dependent vasomotion during sleep promotes glymphatic clearance(16). Moreover, neuromodulatory systems, including cholinergic and adrenergic pathways, can regulate vascular tone and CSF flux, further linking neural activity to fluid transport(17, 18). Together, these findings support a model in which PVS-mediated transport emerges from coupled neurovascular and neurofluid interactions.

Despite these conceptual advances, the anatomical organization and *in vivo* accessibility of PVS across the brain remain poorly resolved. In humans, conventional MRI primarily detects enlarged PVS as macroscopic fluid-filled structures, and recent intrathecal gadolinium (Gd) studies have

begun to visualize periarterial compartments around large vessels, but these approaches remain limited to coarse spatial scales and CSF-accessible regions(19-21). In rodents, contrast-enhanced MRI has demonstrated brain-wide tracer transport following CSF delivery and provided important evidence for CSF-ISF exchange; however, the resulting signals are spatially diffuse and reflect system-level tracer distribution rather than the precise geometry of perivascular spaces surrounding individual vessels(22-25). Optical imaging approaches offer micron-scale resolution but are inherently limited in penetration depth, field of view, and physiological perturbation due to tracer delivery and surgical preparation. As a result, there remains no imaging framework capable of mapping PVS globally while resolving their organization at the level of individual vessels across cortical, subcortical, and deep brain regions *in vivo*.

Despite extensive studies of glymphatic transport, a fundamental question remains unresolved: whether brain-wide perivascular tracer transport is organized according to vascular architecture or simply reflects diffuse tracer movement through tissue. Resolving this question requires an imaging approach capable of following vessel-associated transport continuously from major surface arteries to penetrating cortical vessels and deep brain structures while maintaining whole-brain coverage.

Here, we establish a vessel-resolved MRI approach that enables brain-wide visualization of perivascular tracer transport in vivo. Using this framework, we demonstrate that perivascular tracer transport is hierarchically organized along vascular trees, extending from major cerebral arteries into penetrating vessels and deep subcortical regions. Rather than representing diffuse tracer accumulation, perivascular tracer transport follows a structured vessel-associated organization, with detectable transport confined to a heterogeneous subset of penetrating vessels. These findings provide an anatomical framework for understanding brain-wide neurofluid organization and establish a foundation for investigating how vascular architecture shapes CSF transport in physiology and disease.

Methods

Animals

Adult C57BL/6 mice (4-6 months old; n = 16, 8 males and 8 females) were used in this study. Not all animals were included in every experiment due to region-specific experimental targeting of whole brain versus hippocampal structures. Subsets of animals were analyzed for each experiment, as indicated in the figure legends. Animals used exclusively for RF-coil optimization were not included in the reported totals, as the procedures were part of previously published work. Animals were group-housed (3-4 per cage) under a 12-h light/dark cycle with ad libitum access to food and water. All procedures were approved by the Massachusetts General Hospital Institutional Animal Care and Use Committee (IACUC) and complied with the National Research Council's *Guide for the Care and Use of Laboratory Animals*.

Sample size, replication, and inclusion/exclusion criteria: No statistical methods were used to predetermine sample size. Sample sizes were comparable to those commonly used in ultra-high-field preclinical fMRI studies. Datasets were excluded prior to analysis if animals did not survive scanning, or suboptimal coil placement.

Animal Surgery

RF coil implantation

Mice underwent surgery to affix a custom-built RF coil to the skull. Anesthesia was induced with 5% isoflurane delivered in medical air supplemented with O_2 (15-20%) for 2-3 min, and maintained at 1.5-2.0% isoflurane with respiratory rate used to monitor anesthetic depth. Ophthalmic ointment was applied to protect the corneas, and body temperature was maintained at 37±1 °C using a thermostatically controlled warming pad throughout the procedure. Animals were placed in a stereotaxic frame and secured with ear bars and a bite bar to ensure stable head positioning. Ethiqa XR (buprenorphine extended-release), 3.25 mg/ kg, s.c., was administered once

pre-operatively; per protocol, no additional post-operative analgesia was required due to its prolonged effect.

The scalp was shaved and sterilized with alternating ethanol and iodine swabs. A midline incision was made to expose the skull over the region corresponding to the RF-coil footprint. Residual soft tissue was removed, and the skull surface was cleaned sequentially with 0.3% H_2O_2 and PBS, then allowed to dry. The RF coil was positioned directly over the skull above the targeted brain region, and its tuning was verified at the ^1H Larmor frequency according to 14 T. The coil was temporarily held in place while a thin layer of cyanoacrylate adhesive was applied to bond it to the skull; curing required approximately 5–8 min. Two-part dental cement (Stoelting Co., Wood Dale, IL) was then mixed and applied to encapsulate the coil and exposed bone, taking care to secure the base of the coil firmly and prevent cement from flowing toward the eyes. A craniotomy was made above the right lateral ventricle (LV) under a microscope. A capillary tube filled with 0.25 mmol/mL (250 mM) gadopentetate dimeglumine in sterile 0.9% saline (silica, polyimide-coated smooth tubing, 0.24 mm; DigiKey, MN), pre-connected to a 10-µL microsyringe (WPI, FL), was inserted into the LV at the following coordinates relative to bregma: 0.59 mm caudal, 1.25 mm lateral, and 1.85 mm ventral. After coil fixation and cement placement, the scalp edges were approximated and closed using tissue adhesive. Once the cement had fully hardened (~10 min), the mice were removed from the stereotaxic frame and, while maintained under anesthesia and kept warm, immediately transported for imaging.

Animal preparation for MRI

For MRI experiments, mice were imaged under free-breathing medetomidine anesthesia in combination with low-dose isoflurane. Animals were initially anesthetized with isoflurane (5% induction in medical air with supplemental 15-20% O_2). A subcutaneous bolus of medetomidine (0.05 mg/kg) was then administered; after which, isoflurane was reduced and maintained at 0.5-1.0%, titrated slowly over the course of the imaging session (4-5h total duration) to maintain

physiological stability. Anesthesia was maintained with a continuous low-dose medetomidine infusion (~0.1 mg/kg/h, s.c.). Ophthalmic ointment was applied to protect the cornea, and body temperature was maintained at 37 ±1 °C with a thermostatically regulated warm-air heating system.

In a subset of animals (n = 4), MRI experiments were performed under an alternative anesthesia regimen using ketamine/xylazine (K/X) to validate the robustness of the findings across anesthetic conditions. Mice were anesthetized with an intraperitoneal injection of ketamine (80–100 mg/kg) and xylazine (5–10 mg/kg). Supplemental doses (approximately 20-30% of the initial dose) were administered as needed to maintain a stable anesthetic depth during imaging. Respiration rate and body temperature were continuously monitored, and body temperature was maintained at 37 °C using a thermostatically controlled heating system. Importantly, no qualitative or quantitative differences were observed in the measured imaging outcomes between the medetomidine–isoflurane and K/X anesthesia conditions. Therefore, data from both anesthesia protocols were considered comparable and pooled for analysis.

Animals were positioned in a custom MRI-compatible head holder incorporating ear bars and a bite bar to minimize motion while preserving natural respiration. No paralytics were used. Physiological parameters, including respiration rate and body temperature, were continuously monitored using a small-animal monitoring system throughout the procedure (SA Instruments, NY). Once stable under medetomidine/isoflurane anesthesia, animals were transported into the MRI bore for MR scanning.

MRI methods

MRI systems

All experiments were performed on horizontal bore MRI scanners (Magnex Scientific, UK, 130mm bore size) at the Athinoula A. Martinos Center for Biomedical Imaging (Charlestown, MA, USA).

The 14 T (600 MHz for ^{1}H) system was equipped with a Bruker Avance NEO console running ParaVision 360 v3.3 and a micro-imaging gradient set (Resonance Research, Inc.) providing peak gradient strength of 1.2 T/m over a 60-mm diameter.

Home-built implantable RF coils

Custom implantable RF coils were fabricated in-house on thin PCB substrates following a previously described PCB-based framework. Each coil consisted of a single-loop circular transceiver (≈6 mm diameter) tuned and matched to 50 Ω at the ^{1}H Larmor frequency at 14 T (~600 MHz). Resonance and matching were adjusted using distributed NP0/C0G capacitors on the PCB.

MRI data acquisition

A 3D gradient echo (GE) sequence was used with the following parameters: TR = 80 ms; TE = 2.22 ms; flip angle = 70°; matrix size = 360 × 270 × 320; field of view = 10.8 × 8.1 × 9.6 mm^3; spatial resolution = 30 × 30 × 30 μm^3. The total scan time was approximately 77 min. We first acquired inflow maps, which highlighted vessel voxels as vascular control maps. Subsequently, MION (Molday ION; BioPAL, Inc., Worcester, MA; 10 mg Fe/mL in the manufacturer-supplied aqueous suspension) was administered intravenously via the tail vein at a dose of 5 mg Fe/kg, 5 min before MRI acquisition. Images were then acquired during intraventricular infusion of gadopentetate dimeglumine (0.25 mmol/mL in sterile 0.9% saline; infusion rate, 100 nL/min; total volume, 1–2 μL).

Besides mapping cumulative glymphatic transport using whole-brain imaging, we acquired high-resolution 2D images covering the hippocampus. A 2D GE sequence was used with the following parameters: TR = 120 ms; TE = 2.95 ms; flip angle = 70°; matrix size = 320 × 320; field of view = 6.4 × 6.4 mm^2; in-plane resolution = 20 × 20 μm^2; slice thickness = 250 μm; 2 slices. The total scan time was 7 min 42 s.

For the phase difference map validation, a 3D multi-echo gradient echo (MGE) sequence was used with the following parameters: TR = 80 ms; TE1 = 2.55 ms, TE2 = 6.56 ms; flip angle = 70°; matrix size = 360 × 270 × 320; field of view = 10.8 × 8.1 × 9.6 mm^3; spatial resolution = 30 × 30 × 30 μm^3.

For the Gd-based dynamic contrast-enhanced (DCE) MRI, a multi-slice MGE sequence was used with the following parameters: TR = 80 ms; TE = 2.5, 5.53, 8.56, 11.60, 14.63, and 17.66 ms; flip angle = 75°; matrix size = 256 × 256; field of view = 12.8 × 12.8 mm^2; in-plane resolution = 50 × 50 μm^2; slice thickness = 250 μm; 3 slices; 4 averages; and 150 repetitions.

Data analysis

All MRI data were processed using custom pipelines implemented in MATLAB (MathWorks, Natick, MA) and Analysis of Functional NeuroImages (AFNI) software (NIMH, MD). The analysis framework was designed to systematically identify and quantify perivascular space (PVS) signals relative to vascular structures across multiple spatial scales, while maintaining consistency across animals and imaging conditions. Detailed, figure-specific analysis procedures are provided in the Supplementary Methods.

Vascular structures were first delineated from inflow-sensitive anatomical images and used as spatial references for all subsequent analyses. Gd-enhanced datasets were co-registered to the vascular maps using rigid-body alignment to ensure accurate spatial correspondence between vessels and surrounding perivascular signals. To characterize PVS organization along major vessels, vascular centerlines were extracted and used to define local coordinate systems. Intensity profiles were sampled along directions orthogonal to the vessel axis, enabling quantification of radial signal distributions. Profiles were spatially aligned relative to the vessel center and aggregated across cross-sections and animals to generate population-level estimates of perivascular signal organization.

At the level of cortical penetrating vessels, localized image patches were analyzed to quantify perivascular enhancement relative to adjacent parenchyma. Vessels were segmented based on intensity contrast, and radial signal measurements were obtained from vessel cores and surrounding tissue compartments. Perivascular signal was defined based on relative intensity differences between vessel-adjacent regions and distal tissue. To assess statistical significance, empirical null distributions were generated using randomized spatial sampling, and detection thresholds were defined relative to these controls. To examine laminar organization, measurements were grouped according to cortical depth and analyzed to compare perivascular signal distributions across layers. Depth-dependent profiles were computed by averaging radial signal changes within each cortical compartment.

Temporal dynamics of PVS signal were evaluated by comparing co-registered datasets acquired at multiple time points within the same animals. Vessel-specific measurements were matched across time, enabling paired analyses of perivascular signal evolution following tracer infusion. Similar vessel-resolved segmentation analysis was applied for hippocampal PVS signal quantification. The signal differences across baseline, post-iron, and post-Gd conditions were quantified based on the vessel cores and adjacent perivascular and parenchymal compartments. This approach enabled direct comparison of contrast contributions across imaging conditions while controlling for spatial variability.

To assess whether observed perivascular signals reflected true tracer-related contrast rather than susceptibility-induced artifacts, phase-difference and B_0 field maps were reconstructed from multi-echo data and examined at corresponding spatial locations.

Statistical analyses were performed using paired or unpaired two-tailed t-tests as appropriate. Data are reported as mean ± s.e.m. unless otherwise specified. All analysis procedures were implemented using consistent criteria across datasets without dataset-specific parameter tuning.

Results

Ultra–high-resolution mapping reveals perivascular spaces (PVS) along major cerebral vessels

Using 14 T MRI, we achieved 30 μm isotropic *in vivo* whole-brain imaging in 77 minutes, a spatiotemporal regime not previously attainable with MRI, enabling brain-wide visualization of PVS along major cerebral arteries. By integrating iron-based susceptibility contrast to suppress intravascular signal with intraventricular Gd infusion to selectively enhance CSF compartments, we developed a dual-contrast mapping strategy that enables simultaneous delineation of vascular lumens and adjacent perivascular spaces (PVS) (Fig. 1A). Co-registration of inflow-based MR angiography with Gd-enhanced images revealed a spatial correspondence between hypointense vessel lumens and adjacent hyperintense perivascular signals along major branches of the anterior cerebral artery (ACA). At the level of individual vessels, high-magnification views demonstrated a clear separation between the vessel core and a surrounding ring-like enhancement consistent with PVS (Fig. 1B). Also, Gd-enhanced PVS signals were prominently observed at T-shaped branch points of the ACA-azygos vessels (e.g., Animal 2), suggesting Gd transportation to hierarchical perivascular compartments along major arterial bifurcations. The hierarchical PVS of middle cerebral artery (MCA) were well identified in the ultra-high-resolution dual-contrast images (Supplementary Movie 1).

To quantitatively characterize the spatial relationship between PVS and vessel lumens, we extracted intensity profiles across vessels and their surrounding compartments. The resulting line profiles revealed a sharp central signal dip corresponding to the vessel lumen, flanked by pronounced peaks in the adjacent perivascular regions (Fig. 1C). After normalization, these profiles demonstrated a consistent spatial organization in which perivascular enhancement was confined to regions immediately adjacent to the vessel wall (Fig. 1D). Together, these findings established robust and spatially resolved visualization of PVS along major cerebral vessels at unprecedented *in vivo* resolution.

Layer-resolved characterization of perivascular spaces in cortical penetrating vessels

We next asked whether the dual-contrast framework could resolve PVS associated with intracortical penetrating vessels, which constitute a critical interface for CSF-ISF exchange. Strikingly, high-resolution coronal imaging enabled continuous and unambiguous visualization of PVS along individual penetrating vessels across cortical depth, with perivascular signals tightly co-localized with vessel trajectories (Fig. 2A). This direct, slice-by-slice tracking reveals a coherent vessel-PVS architecture extending from the cortical surface into deeper layers, establishing clear delineation of perivascular compartments at the level of single penetrating vessels.

To enable systematic quantification, we developed an automated pipeline for vessel detection and perivascular segmentation. Vessel lumens were identified using adaptive thresholding to account for local intensity variations, and concentric perivascular layers were generated by iterative morphological dilation, defining radial compartments surrounding each vessel (Fig. 2B). Quantitative analysis was performed across multiple depths along penetrating vessels to ensure robust sampling of perivascular organization. The distribution of perivascular-to-tissue (PV/Tissue) signal ratios revealed a clear deviation from a randomized baseline. Fig. 2C shows that in contrast to the permutation-derived null Gaussian distribution, the observed vessel-based distribution exhibited a pronounced rightward shift, with an excess population in the high-ratio tail. There are approximately 6% of analyzed penetrating-vessel cross-sections to this right-tail excess, exhibiting PV/Tissue ratios exceeding the range predicted by the null distribution. These vessels therefore represent a distinct subset with detectable perivascular enhancement. The absence of a comparable tail in the randomized distribution further supports that this effect reflects structured, vessel-associated signal rather than stochastic variation. Together, these results demonstrate that detectable perivascular tracer accumulation is restricted to a subset of penetrating vessels,

revealing a heterogeneous and non-uniform organization of perivascular pathways across the cortical vasculature.

In addition, layer-resolved signal profiles of the selected penetrating vessels based on the histogram distribution demonstrated a consistent spatial gradient with signal intensity increased from the vessel lumen to inner perivascular layers, followed by a decrease toward surrounding parenchyma (Fig. 2D). The peak perivascular signal intensity exceeding adjacent tissue confirms the presence of detectable PVS compartments at the level of individual penetrating vessels. It should be noted that the size of the vessels showing strong PVS enhancements is not significantly different from the vessels without salient PVS enhancements (Fig. 2E), indicating that this PVS enhanced signals are vessel-size independent, further ruling out magnetic field disturbance-related artifacts. These findings establish that ultra-high-resolution MRI can resolve PVS not only along large surface vessels but also within cortical microvascular networks, with laminar specificity at tens-of-microns scale.

Perivascular enhancement reflects CSF tracer accumulation rather than vascular or susceptibility artifacts

To determine whether the observed perivascular signals reflect CSF tracer accumulation rather than imaging artifacts, we performed controlled experiments that dissociate the effects of iron and Gd agents. During Gd infusion, robust perivascular enhancement was observed surrounding vessels. In contrast, images acquired 3 h post-infusion, after Gd washout but with iron remaining in the vasculature, retained pronounced vessel hypo-intensity while showing a marked loss of perivascular signal (Fig. 3A). Quantitative analysis of matched regions of interest confirmed this dissociation, demonstrating elevated perivascular signal during Gd infusion that returned to baseline following Gd clearance, despite persistent iron-induced signal suppression within vessel lumens (Fig. 3B,C). To further exclude local susceptibility as the source of perivascular enhancement, we compared phase maps with corresponding magnitude images at the level of

individual vessels (Supplementary Fig. 2). There are some vessels exhibiting strong local field offsets, which reflected as pronounced phase shifts, but not showing corresponding perivascular signal enhancement. In contrast, vessels with robust perivascular signal displayed minimal phase perturbation. This direct dissociation indicates that perivascular enhancement is not coupled to local field inhomogeneity and cannot be explained by iron-induced susceptibility effects. Together, these results demonstrate that perivascular enhancement is not attributable to iron-induced susceptibility or flow-related artifacts, but instead reflects the accumulation of Gd-based CSF tracer within PVS compartments.

Multi-scale dynamic mapping links ventricular CSF transport to hippocampal vessel-resolved PVS

To establish the spatiotemporal dynamics of tracer transport following intraventricular delivery, we performed time-resolved mapping of Gd distribution across ventricular and parenchymal compartments. Gd signal rapidly dispersed from the lateral ventricles into surrounding brain regions and persisted over an extended period (~120 min), indicating sustained tracer retention and widespread CSF-ISF exchange (Supplementary Fig. 3, Supplementary Movie 2). These measurements define a mesoscale transport regime characterized by tracer entry from ventricular CSF into brain tissue, in particular, the hippocampal parenchyma, and gradual washout over ~2 hours, establishing a well-defined temporal window during which tracer is present within parenchymal and perivascular compartments.

Within this defined transport window, we next investigated the spatial localization of tracer at the level of individual vessels using a 2D ultra-high-resolution single-vessel imaging scheme(26) (in-plane resolution: 20 × 20 μm²) in the hippocampus. At baseline, hippocampal vessels were detected with hyperintense signals due to the blood inflow effect. Following intravenous iron infusion, blood signals within vessels were markedly attenuated by T2* effects, producing strong hypointensity that clearly delineates vessel lumens in single-vessel maps. Subsequent

intraventricular Gd infusion introduced a distinct and spatially confined enhancement surrounding the vessels, indicating the Gd-enhanced PVS (Fig. 4). This dual-contrast modulation produced a characteristic configuration of dark vessel lumens encircled by bright perivascular rims (Fig. 4A,C), enabling direct separation of vascular and perivascular compartments at the level of individual vessels. Quantitative intensity profiles across inflow, iron, and Gd conditions further confirmed this compartmental dissociation, with peak signal localized to perivascular regions and suppressed within the vessel lumen (Fig. 4D). Together, these results established vessel-resolved detection of hippocampal PVS *in vivo*, linking ventricular CSF tracer transport to a brain-wide PVS network.

Discussion

The present study demonstrates that brain-wide perivascular tracer transport is not spatially diffuse but instead follows a hierarchical organization anchored to the cerebral vascular tree. By achieving vessel-resolved MRI across the whole brain, we show that tracer transport extends continuously from major surface arteries into penetrating cortical vessels and deep brain regions while remaining confined to a heterogeneous subset of vascular pathways. These findings provide an anatomical framework for understanding neurofluid organization in vivo and bridge the gap between macroscopic tracer imaging and vascular-scale organization.

This conceptual advance was enabled by combining ultra-high-field MRI, implantable RF-coil technology, and dual-contrast imaging to separate vascular and perivascular compartments. Rather than simply improving spatial resolution, this approach allows brain-wide neurofluid transport to be examined in relation to vascular architecture at the level of individual vessels.

State of the Art and Limitations of MRI-Based PVS Imaging

Early Gd-enhanced MRI studies in rodents have established that tracers introduced into CSF can access the brain beyond the subarachnoid space, producing widespread parenchymal enhancement and providing initial *in vivo* evidence of CSF-ISF exchange(23-25). Following cisterna magna infusion, contrast agents were observed to enter periarterial pathways along major surface arteries and propagate into deeper brain regions, enabling mapping of brain-wide tracer distribution(23). Subsequent work using quantitative Gd-DOTA imaging and dynamic MRI further characterized the temporal evolution of tracer influx and clearance, demonstrating that a substantial fraction of delivered contrast enters and persists within brain parenchyma(24, 25). More recent studies have shown that these signals reflect global tracer transport dynamics modulated by vascular activity and neuromodulatory state, leading to spatially widespread and diffuse enhancement pattern(17). Despite these advances, the resulting MRI signals primarily reflect system-level tracer distribution rather than the anatomical organization of PVS at the level of individual vessels. A recent in vivo Gd-enhanced MRI study mapped tracer transport along pial periarterial PVS, showing that these spaces can serve as conduits for convective CSF entry into brain tissue(27). This approach primarily captured macroscopic pial PVS flow and downstream tracer distribution, rather than resolving the fine intracortical PVS architecture around penetrating vessels. Notably, emerging high-resolution *in vivo* MRI studies have begun to report vessel-associated signal features, including enhancement patterns localized near hippocampal vessels, suggesting potential sensitivity to perivascular compartments at finer spatial scales(22). However, such signals remain difficult to interpret unambiguously, as prior studies have largely inferred their perivascular origin based on anatomical patterns and disease-related changes, without direct MRI-based suppression or separation of intravascular inflow contributions from hippocampal vessels(26).

In humans, Gd-enhanced MRI has been used to characterize CSF-brain exchange at the whole-brain level, revealing spatially heterogeneous tracer accumulation and clearance over extended

time scales(28). Intrathecal imaging studies further demonstrate tracer propagation along vessel-associated pathways and enhancement in fluid-filled compartments consistent with PVS structures(19, 21). In particular, high-resolution intrathecal MRI has identified circumferential contrast enhancement surrounding major cerebral arteries, consistent with periarterial compartments accessible to CSF transport(20). However, the observed signals remain largely restricted to CSF-accessible compartments and major surface arteries, and are inherently anatomically non-specific. Current human MRI approaches cannot resolve the fine geometry or network-level organization of PVS *in vivo*, nor can they distinguish contributions from vascular, subarachnoid, and interstitial compartments at the level of individual vessels.

Similar limitation applies to *ex vivo* high-resolution MRI studies. While post-mortem imaging following *in vivo* tracer infusion can reveal vessel-associated and ring-like enhancement patterns suggestive of a connected perivascular network(29, 30). These measurements are performed outside physiological conditions and are subject to tracer redistribution, loss of vascular dynamics, and partial-volume effects. Consequently, despite high nominal spatial resolution, these approaches do not provide a definitive *in vivo* framework for resolving the structure and organization of PVS. Together, existing MRI approaches capture brain-wide tracer transport or macroscopic perivascular features, but lack the ability to resolve a vessel-anchored, brain-wide perivascular network *in vivo*.

Vessel-Resolved In Vivo Mapping of PVS Using Dual-Contrast MRI

To overcome these limitations, we developed an ultra-high-resolution dual-contrast MRI framework that enables vessel-resolved mapping of PVS *in vivo* across the whole brain. This capability arises from the combination of ultra-high-field MRI, implantable RF coil for enhanced sensitivity and spatial specificity(31), and Gd-enhanced T1 contrast, which together provide sufficient signal- and contrast-to-noise ratios to resolve perivascular signal at the current spatial scale.

Using this approach, we provided *in vivo* evidence that PVS are hierarchically organized along vascular trees and extend across both surface and deep brain regions. Prominent Gd enhancement observed along the MCA and ACA branches (Fig. 1 and Supplementary Movie 1,5), including characteristic branching geometries such as T-shaped junctions, revealed that PVS follow vascular topology rather than appearing as isolated compartments. At the level of penetrating vessels, quantitative analysis showed that ~6% of vessels exhibit detectable PVS enhancement (Fig. 2), to our knowledge, providing the first vessel-resolved estimate of detectable PVS prevalence under the current imaging conditions across the cortical vasculature. This estimate reflected detectable PVS under the current resolution and contrast conditions, which may underestimate the true prevalence of microscopic PVS. Meanwhile, the vessel diameters associated with detectable PVS were not significantly different from those without enhancement, suggesting that PVS visibility was not determined by vessel caliber or simple flow-related factors, but may instead reflect heterogeneous organization across specific vascular trees. This raises the possibility that PVS were selectively associated with particular vascular pathways, a feature that has not been resolved in prior MRI studies and warrants further investigation.

At the whole-brain level, PVS were observed not only along intracortical vessels but also across subcortical structures, including the hippocampus, midbrain, basal ganglia, and hypothalamic regions (Supplementary Movies 3-5), where they exhibited complex and spatially extended organization. As shown in Fig 4, Gd-enhanced signal was not always confined to a thin annular compartment immediately surrounding the vessel lumen, but could extend into adjacent fluid-filled compartments that remain spatially distinct from vascular signal in the hippocampus, consistent with CSF-accessible spaces rather than blood-derived contrast. This distinction is critical, as prior MRI studies have highlighted the challenge of separating perivascular signal from vascular or inflow-related contributions, and have implemented specific controls to address these confounds(22). In our data, the absence of co-localized susceptibility distortion in phase maps

438 further argues against vascular or susceptibility-related origins (Supplementary Fig. 2). Together,
439 these observations demonstrated the ability of ultra-high-resolution MRI to capture brain-wide
440 perivascular architecture that bridges vascular hierarchies and anatomical domains.

441 A central question raised by these observations is how PVS structures, typically only a few
442 microns wide in optical and histological studies, can be detected at ~30 μm MRI resolution. We
443 do not interpret this as direct visualization of the microscopic PVS boundary. Instead, the
444 observed signal likely reflected a voxel-scale representation of tracer-enriched fluid associated
445 with PVS. The use of ultrashort TE, short TR, and relatively large flip angle enhanced sensitivity
446 to Gd-driven T1 shortening while minimizing iron-induced extravascular susceptibility
447 contamination. In addition, during the prolonged 3D acquisition, Gd was likely sampled not only
448 within the immediate perivascular compartment but also within adjacent fluid-accessible spaces
449 and nearby parenchyma, allowing vessel-associated enhancement to emerge through partial-
450 volume effects. Thus, the detectability of PVS in the present study arises from the combination of
451 strong T1 weighting, reduced susceptibility bias, and spatially organized tracer distribution near
452 vessels, rather than from direct microscopic resolution of a 2-3 μm anatomical space.

453 ***Implications for PVS-Mediated CSF Transport In Vivo***

454 Although the mechanistic basis of glymphatic transport remains under active debate(9, 10, 32),
455 the present work provided an anatomical imaging framework for localizing perivascular tracer
456 dynamics across vascular hierarchies *in vivo*. Following ventricular infusion, Gd contrast rapidly
457 spread from the lateral ventricle into the hippocampal region, with vessel-resolved PVS
458 enhancement detectable by 15 min (Fig. 4, Supplementary Movie 2). These findings
459 demonstrated that tracers introduced into ventricular CSF could access a broadly distributed
460 vessel-associated network, extending into deep cortical and subcortical regions rather than
461 remaining confined to surface pathways(23, 25).

This global, vessel-associated tracer accessibility is consistent with prior models of CSF-ISF exchange, which propose that transport arises from a combination of periarterial pathways, interstitial diffusion, and low-velocity convective components(5, 9, 10, 23, 25, 30, 33-35). Effort to identify the driving forces underlying glymphatic transport suggests that tracer movements with PVS may be influenced by arteria pulsation and or a small net forward component of CSF flow(9, 36). However, theoretical and fluid dynamic analyses indicate that physiological pulsations alone are insufficient to sustain long-range directional transport(34). Instead, solute transport in the brain is more consistently described as a coupled advection-diffusion process shaped by pathway geometry, hydraulic resistance, and exchange between perivascular and interstitial compartments(37, 38).

Consistent with this view, our results demonstrate spatially organized, vessel-selective tracer transport across brain-wide perivascular structures, with only a subset of vessels (~6%) exhibiting detectable PVS enhancement. Also, the use of a relatively low infusion volume and rate (1-2 µl over 10-20 min; 100nl/min) reduces the likelihood that the observed global PVS enhancement is dominated by infusion-driven perturbations. Nonetheless, even low-volume ventricular infusion can alter intracranial pressure and influence pathway recruitment, and tracer distribution is known to be sensitive to infusion conditions and physiological state(9, 33, 34, 36, 39). Accordingly, our findings are best interpreted not as a direct measurement of unperturbed physiological CSF flow, but as evidence that PVS-associated tracer transport can be detected globally and anatomically localized *in vivo* under relatively mild perturbation conditions.

Limitations and technical considerations

Several technical considerations should be noted when interpreting the present findings. First, the use of intravascular iron contrast introduces local susceptibility effects that influence both vascular and perivascular signal measurements. While iron-induced T2* shortening effectively suppresses intravascular inflow signals, facilitating separation of vessel lumens from surrounding

compartments, it also generates local magnetic field perturbations that extend into the extravascular space. These susceptibility effects may partially attenuate Gd-enhanced perivascular signals and reduce local CNR. Although the use of short echo times and ultra-high spatial resolution mitigates these effects, residual susceptibility-induced bias is likely to persist, potentially leading to an underestimation of detectable PVS across the vascular population. Second, although multiple lines of evidence support that the observed perivascular enhancement reflects true tracer accumulation rather than susceptibility-related artifacts, complete exclusion of all confounding effects remains challenging. Several observations argue against a susceptibility-driven origin. The spatial organization of perivascular signal along vascular trees, including characteristic branching patterns such as T-shaped structures along ACA branches or penetrating vessel branches in deep brain regions, is not consistent with local field distortion. In addition, the detection of PVS is independent of vessel size, further arguing against susceptibility-driven contrast, which would scale with vessel caliber. Finally, perivascular enhancement is abolished following Gd washout at ~3 h, whereas iron-induced vascular hypointensity persists, indicating dissociation between susceptibility effects and perivascular signal. Together, these findings support a tracer-based origin of the observed PVS signals, although subtle interactions between susceptibility and T1-weighted contrast cannot be entirely excluded. Third, the present framework primarily provides a structural and quasi-static mapping of perivascular tracer distribution, rather than a direct measurement of dynamic CSF flow within PVS. Capturing the spatiotemporal dynamics of tracer transport at the level of individual vessels would require substantially higher temporal resolution while maintaining mesoscale spatial resolution, which remains technically challenging. Although Gd-induced T1 shortening enhances sensitivity to CSF-associated signal, achieving sufficient CNR for resolving low-velocity flow within narrow perivascular compartments remains difficult. Future developments combining accelerated acquisition strategies with vessel-targeted analysis may enable slice-selective or vessel-resolved measurements of CSF transport along defined vascular trajectories.

Together, these findings establish a previously unavailable anatomical framework for resolving perivascular tracer dynamics across the brain *in vivo*. By enabling vessel-resolved mapping of PVS across vascular hierarchies, this approach bridges global tracer imaging and mechanistic models of CSF transport. This framework provides a foundation for future studies aimed at disentangling the relative contributions of pressure-driven flow, pulsation, diffusion, and pathway-specific resistance in brain fluid transport.

Conclusions

By combining ultra-high-field MRI, an implantable radiofrequency coil, and dual-contrast imaging, we establish a vessel-resolved framework for mapping brain-wide perivascular tracer distribution in vivo. Our findings reveal a hierarchical organization of vessel-associated tracer enhancement, extending from major surface arteries to cortical penetrating vessels and deep brain regions, including the hippocampus. Detectable perivascular enhancement was confined to a heterogeneous subset of penetrating vessels under the present imaging conditions, highlighting the spatial selectivity of tracer accessibility. Importantly, this approach maps tracer distribution and accumulation rather than directly measuring CSF flow velocity or direction within perivascular spaces. Together, these findings provide an anatomical framework for investigating the organization and physiological regulation of brain fluid transport in health and disease.

List of abbreviations

ACA, anterior cerebral artery; AFNI, Analysis of Functional NeuroImages; CNR, contrast-to-noise ratio; CSF, cerebrospinal fluid; DCE, dynamic contrast-enhanced; FOV, field of view; Gd, gadolinium; GE, gradient echo; GRE, gradient-recalled echo; ISF, interstitial fluid; K/X, ketamine/xylazine; LV, lateral ventricle; MCA, middle cerebral artery; MGE, multi-echo gradient echo; MION, monocrystalline iron oxide nanoparticle; MRI, magnetic resonance imaging; PVS, perivascular space(s); RF, radiofrequency; ROI, region of interest; TE, echo time; TR, repetition time.

Declarations

Ethics approval and consent to participate

All animal procedures were approved by the Massachusetts General Hospital Institutional Animal Care and Use Committee (IACUC) and complied with the National Research Council's Guide for the Care and Use of Laboratory Animals. Consent to participate: not applicable (animal study).

Consent for publication

Not applicable. No identifiable individual human data are reported.

Availability of data and materials

The datasets generated and/or analyzed during the current study are available from the corresponding authors on reasonable request.

Code availability

The custom code used for data processing and analysis is available from the corresponding authors upon reasonable request.

Competing interests

The authors declare no competing interests.

Funding

This work was supported by the Alzheimer's Association (ARFD-23-1145375 to X.A.Z.), the Brain & Behavior Research Foundation Young Investigator Award (to X.A.Z.), and NIH grant (R01AG094755 to X.A.Z). Additional support was provided by NIH grants (RF1NS124778, R01NS122904, U19NS123717), NSF grant 2123971, and the S10 instrumentation grants (S10MH124733, S10OD036211) to the Martinos Center.

Authors' contributions

X.A.Z. and X.Y. conceived and designed the study. X.A.Z., X.L., W.M., S.C.C., D.H., X.W., and Y.J. contributed to experimental data acquisition and analysis. M.N., K.T.K., and B.B. contributed to scientific interpretation and critical revision of the manuscript. X.A.Z. drafted the manuscript with input from X.Y. All authors read and approved the final manuscript.

Acknowledgements

Not applicable.

Figure Legends

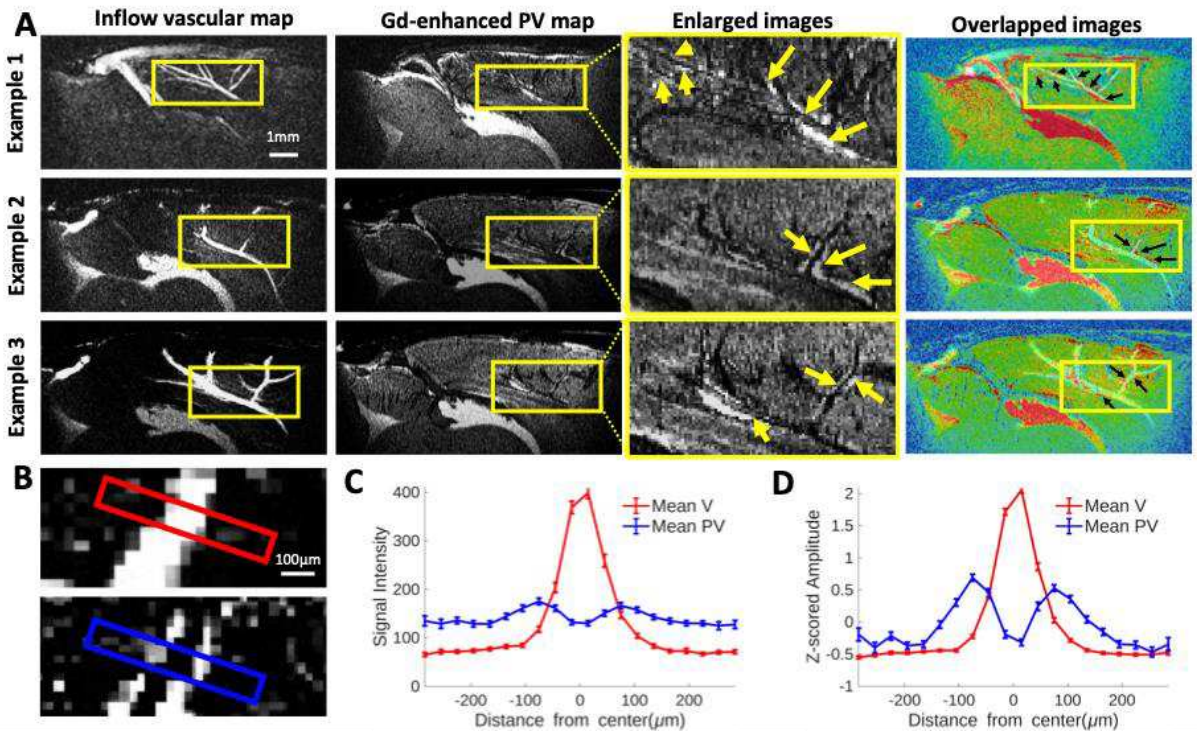


Figure 1. Ultra-high-resolution visualization of PVS along major cerebral arteries

A, Co-registered inflow-based vascular map (V), Gd-enhanced perivascular (PV) map, and their overlap demonstrate spatial correspondence between vessel lumens and adjacent perivascular

spaces along major branches of the anterior cerebral artery (ACA) across animals (3 examples). Iron-based contrast suppresses intravascular signal, rendering vessels hypointense, while Gd infusion selectively enhances perivascular compartments (Enlarged images: arrows indicate Gd-enhanced PVS structure).

B, Representative magnified view of a single ACA (azygos) vessel and its surrounding PVS. The top panel shows the inflow vascular image, and the bottom panel shows the corresponding Gd-enhanced PV image. Line profiles were extracted along the indicated axes (red and blue lines) over a 20-voxel segment (±10 voxels from vessel center; voxel size = 30 μm).

C, Averaged radial intensity profiles from 150 accepted vessel cross-sections sampled along major ACA branches in 9 animals, showing spatial signal distribution from the vessel lumen (center) to surrounding perivascular regions. Profiles reveal a central hypointense vascular core flanked by enhanced perivascular signal.

D, Normalized intensity profiles corresponding to (C), highlighting consistent spatial organization of vessel and perivascular signals independent of absolute intensity differences.

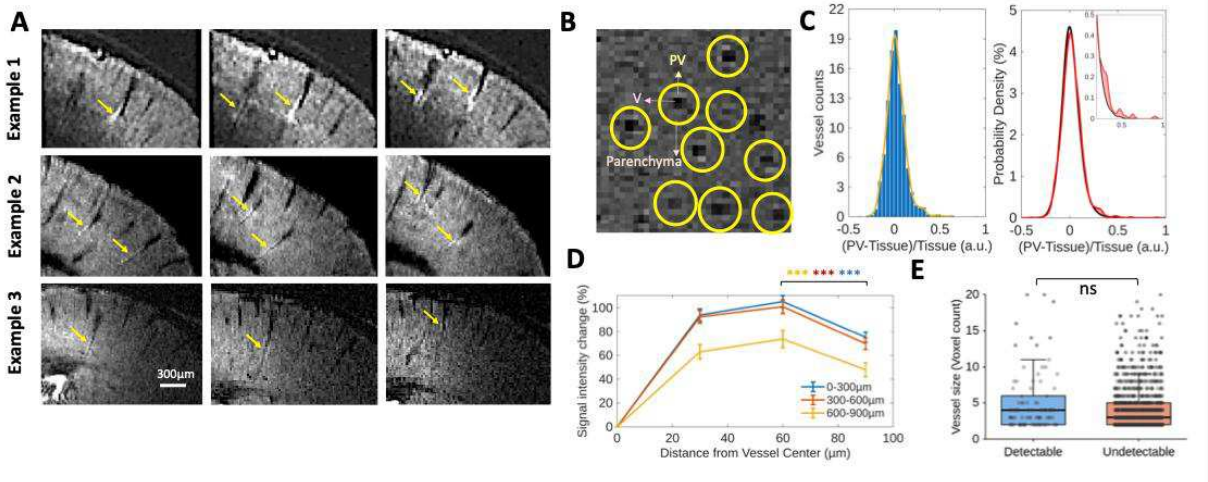


Figure 2. Layer-resolved characterization of PVS in cortical penetrating vessels

A, Representative coronal views showing penetrating cortical vessels and associated perivascular signals across animals. Arrows indicate vessel trajectories and adjacent PVS along cortical depth.

B, Schematic of region-of-interest (ROI) selection and analysis workflow. The underlying image shows an axial view of cortical penetrating vessels. Vessel lumens were segmented using adaptive thresholding. Concentric perivascular layers were generated by iterative dilation (layer thickness: 30-60 μm), and surrounding parenchyma was defined as regions located 90 μm from the vessel boundary.

C, Distribution of perivascular signal contrast across segmented vessel cross-sections (n = 1,564 cross-sections from 8 animals). The left panel shows the empirical histogram of vessel-wise contrast values. The right panel compares the kernel density estimate of the observed distribution (red) with the position-randomized null distribution (black), generated from 1,000 randomizations. The detection threshold was defined as the 95th percentile of the null distribution. The inset highlights the right-tail portion of the observed distribution exceeding this threshold.

D, Mean signal intensity profiles across vessel cross-sections derived from vessels with detectable PVS signal at three cortical depths (0–300, 300–600 and 600–900 μm from the pial surface; surface, middle and bottom layers). Signal profiles were sampled perpendicular to the vessel axis to obtain cross-sectional measurements. Data are presented as mean ± SEM (n = 237 vessels from 8 animals, $p<0.001$, FDR-corrected), showing elevated perivascular signal relative to the vessel lumen and surrounding parenchyma across depths.

E, Comparison of segmented vessel-mask area distributions between cross-sections with and without detectable PVS enhancement. Each dot represents one vessel cross-section. No significant difference was detected between PVS-detectable cross-sections (n = 90; median = 4 voxels) and PVS-undetectable cross-sections (n = 1,444; median = 3 voxels; two-sample

Kolmogorov–Smirnov test, p = 0.3346). Of the 1,564 cross-sections analyzed in C, 30 with vessel-mask areas exceeding 20 in-plane voxels were excluded.

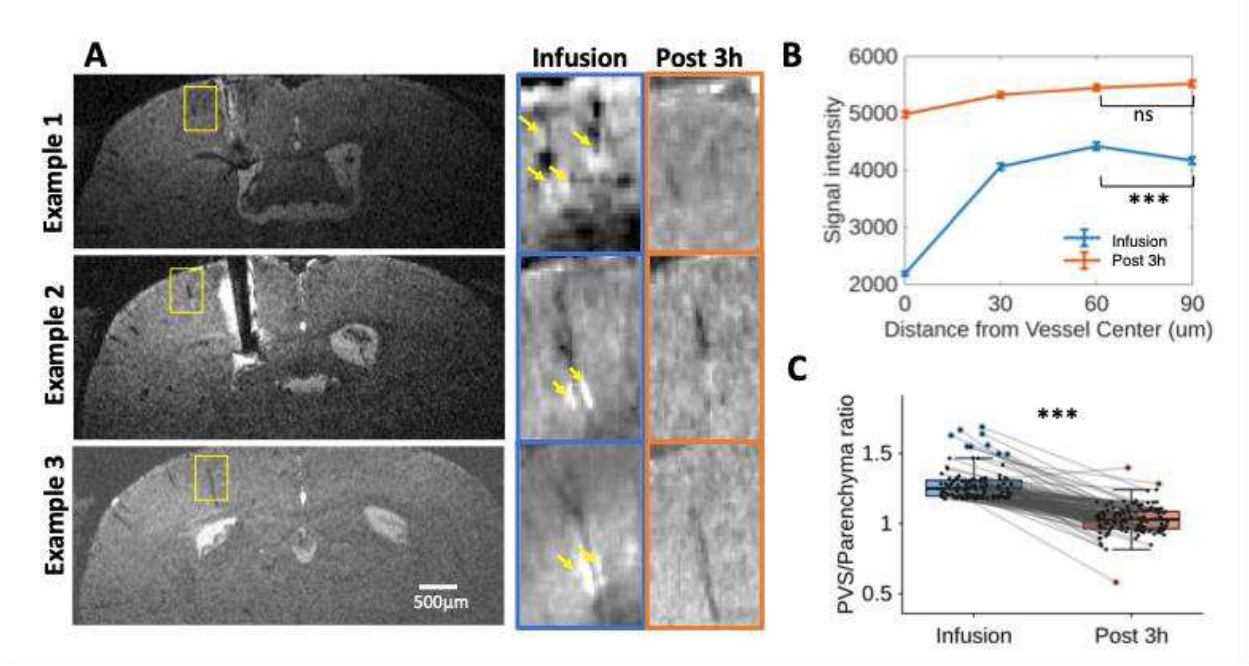


Figure 3. Perivascular enhancement arises from CSF tracer accumulation rather than susceptibility artifacts

A, Representative high-resolution MR images acquired during Gd infusion (left, blue) and 3 h post-infusion (right, orange) across animals. Yellow boxes indicate regions containing penetrating vessels. Vessel lumens remain hypointense in both conditions due to persistent iron contrast, whereas perivascular enhancement is observed only during Gd infusion and is absent after Gd washout.

B, Mean signal intensity profiles across vessel lumen and concentric perivascular layers for the two conditions. Data are presented as mean ± SEM (n = 200 vessels from 8 animals). Perivascular signal is significantly higher during Gd infusion compared to 3 h post-infusion at matched distances from the vessel center (*P < 0.001, FDR-corrected), while vascular contrast remains

unchanged, confirming that PVS enhancement reflects CSF tracer accumulation rather than iron-induced or flow-related artifacts.

C, Perivascular-to-parenchyma signal ratio for individual vessels during Gd infusion and 3 h post-infusion. Data are presented as mean ± SEM (n = 200 vessels from 8 animals). Each dot represents one vessel. The PV/parenchyma ratio is significantly higher during infusion compared to post-infusion (*P < 0.001), and decreases following Gd clearance, indicating that perivascular enhancement reflects transient CSF tracer accumulation.

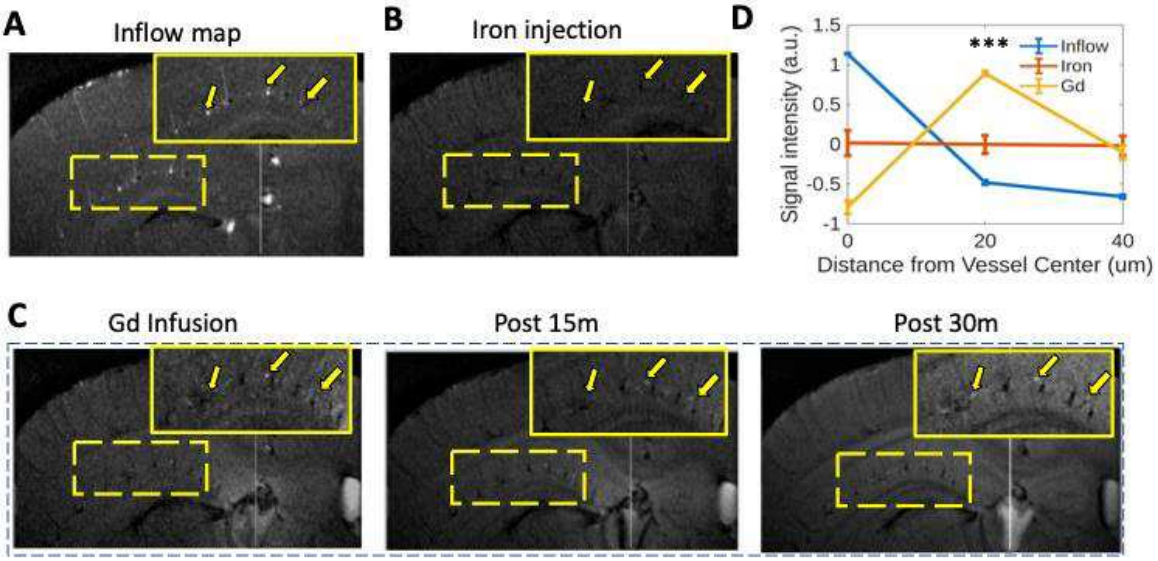


Figure 4. Dynamic contrast modulation separates vascular and perivascular signal components in penetrating vessels

A-C, Sequential MR images acquired at baseline (**A**), after iron infusion (**B**), and after Gd infusion (**C**) demonstrate distinct signal contributions from vascular and perivascular compartments. At baseline, vessels exhibit strong inflow signal; following iron infusion, vessels become hypointense

due to T2* effects; subsequent Gd infusion produces localized enhancement surrounding the vessel, consistent with perivascular space labeling. Yellow boxes highlight representative regions. **D**, Mean signal intensity profiles across vessel-centered ROIs for the three conditions. Data are presented as mean ± SEM (n = 38 vessels from 8 animals). Iron selectively suppresses intravascular signal, whereas Gd selectively enhances perivascular compartments, enabling clear separation of vascular and perivascular signals. Perivascular signal under Gd is significantly higher than both inflow and iron conditions ($P < 0.001$, FDR-corrected).

References

1. Virchow R. Ueber die Erweiterung kleinerer Gefäfse. Archiv für pathologische Anatomie und Physiologie und für klinische Medicin. 1851;3(3):427-62.
2. Robin C. Recherches sur quelques particularites de la structure des capillaires de l'encephale. J Physiol Homme Animaux. 1859;2:537.
3. Ineichen BV, Okar SV, Proulx ST, Engelhardt B, Lassmann H, Reich DS. Perivascular spaces and their role in neuroinflammation. Neuron. 2022;110(21):3566-81.
4. Iliff JJ, Wang M, Liao Y, Plogg BA, Peng W, Gundersen GA, et al. A Paravascular Pathway Facilitates CSF Flow Through the Brain Parenchyma and the Clearance of Interstitial Solutes, Including Amyloid β. Science Translational Medicine. 2012;4(147):147ra11-ra11.
5. Carare RO, Bernardes-Silva M, Newman TA, Page AM, Nicoll JA, Perry VH, et al. Solutes, but not cells, drain from the brain parenchyma along basement membranes

of capillaries and arteries: significance for cerebral amyloid angiopathy and neuroimmunology. Neuropathol Appl Neurobiol. 2008;34(2):131-44.

6. Carare RO. Intramural Peri Arterial Drainage (IPAD) of peptides from the brain parenchyma and retina. Alzheimer's & Dementia. 2025;21(S1):e100903.

7. Albargothy NJ, Johnston DA, MacGregor-Sharp M, Weller RO, Verma A, Hawkes CA, et al. Convective influx/glymphatic system: tracers injected into the CSF enter and leave the brain along separate periarterial basement membrane pathways. Acta neuropathologica. 2018;136(1):139-52.

8. Wardlaw JM, Benveniste H, Nedergaard M, Zlokovic BV, Mestre H, Lee H, et al. Perivascular spaces in the brain: anatomy, physiology and pathology. Nat Rev Neurol. 2020;16(3):137-53.

9. Mestre H, Mori Y, Nedergaard M. The Brain's Glymphatic System: Current Controversies. Trends in neurosciences. 2020;43(7):458-66.

10. Hladky SB, Barrand MA. The glymphatic hypothesis: the theory and the evidence. Fluids Barriers CNS. 2022;19(1):9.

11. Hablitz LM, Plá V, Giannetto M, Vinitsky HS, Stæger FF, Metcalfe T, et al. Circadian control of brain glymphatic and lymphatic fluid flow. Nature communications. 2020;11(1):4411.

12. Fultz NE, Bonmassar G, Setsompop K, Stickgold RA, Rosen BR, Polimeni JR, et al. Coupled electrophysiological, hemodynamic, and cerebrospinal fluid oscillations in human sleep. Science. 2019;366(6465):628-31.

13. Jiang-Xie L-F, Drieu A, Bhasiin K, Quintero D, Smirnov I, Kipnis J. Neuronal dynamics direct cerebrospinal fluid perfusion and brain clearance. Nature. 2024;627(8002):157-64.

14. Holstein-Rønsbo S, Gan Y, Giannetto MJ, Rasmussen MK, Sigurdsson B, Beinlich FRM, et al. Glymphatic influx and clearance are accelerated by neurovascular coupling. Nature neuroscience. 2023;26(6):1042-53.

15. Mestre H, Tithof J, Du T, Song W, Peng W, Sweeney AM, et al. Flow of cerebrospinal fluid is driven by arterial pulsations and is reduced in hypertension. Nature communications. 2018;9(1):4878.

16. Hauglund NL, Andersen M, Tokarska K, Radovanovic T, Kjaerby C, Sørensen FL, et al. Norepinephrine-mediated slow vasomotion drives glymphatic clearance during sleep. Cell. 2025;188(3):606-22.e17.

17. Chuang K-H, Zhou XA, Xia Y, Li Z, Qian L, Eeles E, et al. Cholinergic basal forebrain neurons regulate vascular dynamics and cerebrospinal fluid flux. Nature communications. 2025;16(1):5343.

18. Sun Q, Peng S, Xu Q, Weikop P, Hussain R, Song W, et al. Enhancing glymphatic fluid transport by pan-adrenergic inhibition suppresses epileptogenesis in male mice. Nature communications. 2024;15(1):9600.

19. Naganawa S, Nakane T, Kawai H, Taoka T. Gd-based Contrast Enhancement of the Perivascular Spaces in the Basal Ganglia. Magn Reson Med Sci. 2017;16(1):61-5.

20. Eide PK, Ringstad G. Functional analysis of the human perivascular subarachnoid space. Nature communications. 2024;15(1):2001.

21. Yamamoto EA, Bagley JH, Geltzeiler M, Sanusi OR, Dogan A, Liu JJ, et al. The perivascular space is a conduit for cerebrospinal fluid flow in humans: A proof-of-principle report. Proceedings of the National Academy of Sciences. 2024;121(42):e2407246121.

22. Monte B, Constantinou S, Koundal S, Lee H, Dai F, Gursky Z, et al. Characterization of perivascular space pathology in a rat model of cerebral small vessel disease by in vivo magnetic resonance imaging. Journal of Cerebral Blood Flow & Metabolism. 2022;42(10):1813-26.

23. Iliff JJ, Lee H, Yu M, Feng T, Logan J, Nedergaard M, et al. Brain-wide pathway for waste clearance captured by contrast-enhanced MRI. The Journal of clinical investigation. 2013;123(3):1299-309.

24. Lee H, Mortensen K, Sanggaard S, Koch P, Brunner H, Quistorff B, et al. Quantitative Gd-DOTA uptake from cerebrospinal fluid into rat brain using 3D VFA-SPGR at 9.4T. Magnetic resonance in medicine : official journal of the Society of Magnetic Resonance in Medicine / Society of Magnetic Resonance in Medicine. 2018;79(3):1568-78.

25. Stanton EH, Persson NDÅ, Gomolka RS, Lilius T, Sigurðsson B, Lee H, et al. Mapping of CSF transport using high spatiotemporal resolution dynamic contrast-enhanced MRI in mice: Effect of anesthesia. Magnet Reson Med. 2021;85(6):3326-42.

26. Chen X, Sobczak F, Chen Y, Jiang Y, Qian C, Lu Z, et al. Mapping optogenetically-driven single-vessel fMRI with concurrent neuronal calcium recordings in the rat hippocampus. Nature communications. 2019;10(1):5239.

27. Mortensen KN, Lilius T, Rosenholm M, Sigurðsson B, Kelley DH, Nedergaard M. Perivascular cerebrospinal fluid inflow matches interstitial fluid efflux in anesthetized rats. iScience. 2025;28(5):112323.
28. Watts R, Steinklein JM, Waldman L, Zhou X, Filippi CG. Measuring Glymphatic Flow in Man Using Quantitative Contrast-Enhanced MRI. AJNR American journal of neuroradiology. 2019;40(4):648-51.
29. Magdoom KN, Brown A, Rey J, Mareci TH, King MA, Sarntinoranont M. MRI of Whole Rat Brain Perivascular Network Reveals Role for Ventricles in Brain Waste Clearance. Scientific reports. 2019;9(1):11480.
30. Rey JA, Farid UM, Najjoum CM, Brown A, Magdoom KN, Mareci TH, et al. Perivascular network segmentations derived from high-field MRI and their implications for perivascular and parenchymal mass transport in the rat brain. Scientific reports. 2023;13(1):9205.
31. Hike D, Liu X, Xie Z, Zhang B, Choi S, Zhou XA, et al. High-resolution awake mouse fMRI at 14 tesla. eLife. 2025;13:RP95528.
32. Zhao L, Tannenbaum A, Bakker E, Benveniste H. Physiology of Glymphatic Solute Transport and Waste Clearance from the Brain. Physiology (Bethesda). 2022;37(6):0.
33. Smith AJ, Yao X, Dix JA, Jin B-J, Verkman AS. Test of the 'glymphatic' hypothesis demonstrates diffusive and aquaporin-4-independent solute transport in rodent brain parenchyma. eLife. 2017;6:e27679.
34. Kedarasetti RT, Drew PJ, Costanzo F. Arterial pulsations drive oscillatory flow of CSF but not directional pumping. Scientific reports. 2020;10(1):10102.

753 35. Morris AW, Sharp MM, Albargothy NJ, Fernandes R, Hawkes CA, Verma A, et al.
754 Vascular basement membranes as pathways for the passage of fluid into and out of the
755 brain. Acta neuropathologica. 2016;131(5):725-36.
756 36. Bedussi B, Almasian M, de Vos J, VanBavel E, Bakker EN. Paravascular spaces
757 at the brain surface: Low resistance pathways for cerebrospinal fluid flow. Journal of
758 cerebral blood flow and metabolism : official journal of the International Society of
759 Cerebral Blood Flow and Metabolism. 2018;38(4):719-26.
760 37. Ray LA, Heys JJ. Fluid Flow and Mass Transport in Brain Tissue. Fluids
761 [Internet]. 2019; 4(4):[196 p.].
762 38. Ray L, Iliff JJ, Heys JJ. Analysis of convective and diffusive transport in the brain
763 interstitium. Fluids and Barriers of the CNS. 2019;16(1):6.
764 39. Raghunandan A, Ladron-de-Guevara A, Tithof J, Mestre H, Du T, Nedergaard M,
765 et al. Bulk flow of cerebrospinal fluid observed in periarterial spaces is not an artifact of
766 injection. Elife. 2021;10.
767

Supplementary Files

This is a list of supplementary files associated with this preprint. Click to download.

- SupplementaryMethods.pdf
- SuppMovie5.mp4
- SuppMovie2.mp4
- SuppMovie1.mp4
- SuppMovie3.mp4
- SuppMovie4.mp4